Birefringence measurement of cornea and anterior segment by office-based polarization-sensitive optical coherence tomography

Yiheng Lim,[1,4] Masahiro Yamanari,[1,4] Shinichi Fukuda,[2,4] Yuichi Kaji,[2,4] Takahiro Kiuchi,[2,4] Masahiro Miura,[3,4] Tetsuro Oshika[2,4] and Yoshiaki Yasuno[1,4,*]

[1]*Computational Optics Group in the University of Tsukuba, Tsukuba, Japan*
[2]*Department of Ophthalmology, Institute of Clinical Medicine, University of Tsukuba, Tsukuba, Japan*
[3]*Department of Ophthalmology, Ibaraki Medical Center, Tokyo Medical University, Ami, Japan*
[4]*Computational Optics and Ophthalmology Group, Tsukuba, Japan*
*yasuno@optlab2.bk.tsukuba.ac.jp

Abstract: We present a case series of cornea and anterior segment disorders investigated by an office-based polarization-sensitive optical coherence tomography (PS-OCT). Blebs of glaucoma patients treated by trabeculectomy, and corneas of keratoconus and keratoplasty patients were measured by PS-OCT. Birefringence formations in trabeculectomy bleb were measured in 1 control eye and 3 eyes of trabeculectomy model rabbits. Polarization insensitive scattering OCT and the depth-resolved birefringence were measured simultaneously by PS-OCT. Abnormal birefringence was observed in keratoconus cases with advanced thinning and with a rupture of Descemet's membrane. The graft-host interface of the keratoplasty case showed abnormal birefringence. The appearance of abnormal birefringence in the cornea was likely to be an indication of cross-linking of collagen fibrils. The measurement of rabbit showed abnormal birefringence in the scarring eyes. Wide regions of strong birefringence were observed in the eyes of trabeculectomy patients who had high intraocular pressure. Visualization of scarring in bleb by PS-OCT may be useful for the planning of secondary surgery. PS-OCT showed promising for the study and diagnosis diseases related to abnormal fibrous tissues of the cornea and anterior eye segment.

References and links

1. D. Huang, E. A. Swanson, C. P. Lin, J. S. Schuman, W. G. Stinson, W. Chang, M. R. Hee, T. Flotte, K. Gregory, C. A. Puliafito, and J. G. Fujimoto, "Optical coherence tomography," Science **254**(5035), 1178–1181 (1991).
2. J. A. Izatt, M. R. Hee, E. A. Swanson, C. P. Lin, D. Huang, J. S. Schuman, C. A. Puliafito, and J. G. Fujimoto, "Micrometer-scale resolution imaging of the anterior eye *in vivo* with optical coherence tomography," Arch. Ophthalmol. **112**(12), 1584–1589 (1994).
3. A. G. Podoleanu and R. B. Rosen, "Combinations of techniques in imaging the retina with high resolution," Prog. Retin. Eye Res. **27**(4), 464–499 (2008), http://dx.doi.org/10.1016/j.preteyeres.2008.03.002.
4. J. F. de Boer and T. E. Milner, "Review of polarization sensitive optical coherence tomography and Stokes vector determination," J. Biomed. Opt. **7**(3), 359–371 (2002).
5. B. Cense, T. C. Chen, B. H. Park, M. C. Pierce, and J. F. de Boer, "Thickness and birefringence of healthy retinal nerve fiber layer tissue measured with polarization-sensitive optical coherence tomography," Invest. Ophthalmol. Vis. Sci. **45**(8), 2606–2612 (2004).
6. M. Yamanari, M. Miura, S. Makita, T. Yatagai, and Y. Yasuno, "Phase retardation measurement of retinal nerve fiber layer by polarization-sensitive spectral-domain optical coherence tomography and scanning laser polarimetry," J. Biomed. Opt. **13**(1), 014013 (2008).
7. M. Pircher, E. Götzinger, O. Findl, S. Michels, W. Geitzenauer, C. Leydolt, U. Schmidt-Erfurth, and C. K. Hitzenberger, "Human macula investigated in vivo with polarization-sensitive optical coherence tomography," Invest. Ophthalmol. Vis. Sci. **47**(12), 5487–5494 (2006).

8.   M. Miura, M. Yamanari, T. Iwasaki, A. E. Elsner, S. Makita, T. Yatagai, and Y. Yasuno, "Imaging polarimetry in age-related macular degeneration," Invest. Ophthalmol. Vis. Sci. **49**(6), 2661–2667 (2008).
9.   E. Götzinger, M. Pircher, W. Geitzenauer, C. Ahlers, B. Baumann, S. Michels, U. Schmidt-Erfurth, and C. K. Hitzenberger, "Retinal pigment epithelium segmentation by polarization sensitive optical coherence tomography," Opt. Express **16**(21), 16410–16422 (2008).
10.   A. Miyazawa, M. Yamanari, S. Makita, M. Miura, K. Kawana, K. Iwaya, H. Goto, and Y. Yasuno, "Tissue discrimination in anterior eye using three optical parameters obtained by polarization sensitive optical coherence tomography," Opt. Express **17**(20), 17426–17440 (2009).
11.   F. G. Schlanitz, B. Baumann, T. Spalek, C. Schütze, C. Ahlers, M. Pircher, E. Götzinger, C. K. Hitzenberger, and U. Schmidt-Erfurth, "Performance of automated drusen detection by polarization-sensitive optical coherence tomography," Invest. Ophthalmol. Vis. Sci. 52(7), 4571–4579 (2011).
12.   Y. Zhang, Q. Wu, M. Zhang, B. W. Song, X. H. Du, and B. Lu, "Evaluating subconjunctival bleb function after trabeculectomy using slit-lamp optical coherence tomography and ultrasound biomicroscopy," Chin. Med. J. (Engl.) **121**(14), 1274–1279 (2008).
13.   M. Singh, P. T. Chew, D. S. Friedman, W. P. Nolan, J. L. See, S. D. Smith, C. Zheng, P. J. Foster, and T. Aung, "Imaging of trabeculectomy blebs using anterior segment optical coherence tomography," Ophthalmology **114**(1), 47–53 (2007).
14.   K. Kawana, T. Kiuchi, Y. Yasuno, and T. Oshika, "Evaluation of trabeculectomy blebs using 3-dimensional cornea and anterior segment optical coherence tomography," Ophthalmology **116**(5), 848–855 (2009).
15.   M. Miura, K. Kawana, T. Iwasaki, T. Kiuchi, T. Oshika, H. Mori, M. Yamanari, S. Makita, T. Yatagai, and Y. Yasuno, "Three-dimensional anterior segment optical coherence tomography of filtering blebs after trabeculectomy," J. Glaucoma **17**(3), 193–196 (2008).
16.   A. Labbé, B. Dupas, P. Hamard, and C. Baudouin, "*In vivo* confocal microscopy study of blebs after filtering surgery," Ophthalmology **112**(11), 1979.e1–1979.e9 (2005).
17.   Y. Yasuno, M. Yamanari, K. Kawana, T. Oshika, and M. Miura, "Investigation of post-glaucoma-surgery structures by three-dimensional and polarization sensitive anterior eye segment optical coherence tomography," Opt. Express **17**(5), 3980–3996 (2009).
18.   A. Stanworth and E. J. Naylor, "Polarized light studies of the cornea: I. the isolated cornea," J. Exp. Biol. **30**, 160–163 (1953).
19.   G. J. Van Blokland and S. C. Verhelst, "Corneal polarization in the living human eye explained with a biaxial model," J. Opt. Soc. Am. A **4**(1), 82–90 (1987).
20.   J. M. Bueno and F. Vargas-Martín, "Measurements of the corneal birefringence with a liquid-crystal imaging polariscope," Appl. Opt. **41**(1), 116–124 (2002).
21.   J. W. Jaronski and H. T. Kasprzak, "Linear birefringence measurements of the in vitro human cornea," Ophthalmic Physiol. Opt. **23**(4), 361–369 (2003).
22.   E. Götzinger, M. Pircher, M. Sticker, A. F. Fercher, and C. K. Hitzenberger, "Measurement and imaging of birefringent properties of the human cornea with phase-resolved, polarization-sensitive optical coherence tomography," J. Biomed. Opt. **9**(1), 94–102 (2004).
23.   R. A. Bone and G. Draper, "Optical anisotropy of the human cornea determined with a polarizing microscope," Appl. Opt. **46**(34), 8351–8357 (2007).
24.   F. Fanjul-Vélez, M. Pircher, B. Baumann, E. Götzinger, C. K. Hitzenberger, and J. L. Arce-Diego, "Polarimetric analysis of the human cornea measured by polarization-sensitive optical coherence tomography," J. Biomed. Opt. **15**(5), 056004 (2010).
25.   E. Götzinger, M. Pircher, I. Dejaco-Ruhswurm, S. Kaminski, C. Skorpik, and C. K. Hitzenberger, "Imaging of birefringent properties of keratoconus corneas by polarization-sensitive optical coherence tomography," Invest. Ophthalmol. Vis. Sci. **48**(8), 3551–3558 (2007).
26.   M. Yamanari, S. Makita, and Y. Yasuno, "Polarization-sensitive swept-source optical coherence tomography with continuous source polarization modulation," Opt. Express **16**(8), 5892–5906 (2008).
27.   S. Makita, M. Yamanari, and Y. Yasuno, "Generalized Jones matrix optical coherence tomography: performance and local birefringence imaging," Opt. Express **18**(2), 854–876 (2010).
28.   M. Yamanari, S. Makita, Y. Lim, and Y. Yasuno, "Full-range polarization-sensitive swept-source optical coherence tomography by simultaneous transversal and spectral modulation," Opt. Express **18**(13), 13964–13980 (2010).
29.   B. Baumann, E. Götzinger, M. Pircher, and C. K. Hitzenberger, "Single camera based spectral domain polarization sensitive optical coherence tomography," Opt. Express **15**(3), 1054–1063 (2007).

1. Introduction

Optical coherence tomography (OCT) is a non-contact and non-invasive imaging technology that visualizes a cross-sectional and three-dimensional structure of a biological tissue at micrometer resolution [1]. OCT has been used for ophthalmic imaging, and is indispensable for the diagnosis of many ocular diseases [2,3]. Polarization-sensitive OCT (PS-OCT), which is one of the functional extensions of OCT, can improve the image contrast of OCT by imaging birefringence of biological fibrous tissues [4]. PS-OCT has been demonstrated to discriminate between ocular tissues using their birefringence properties in studies on the

posterior segment of the eye, retinal nerve fiber [5,6] and scar tissue in age-related macular degeneration [7,8]. Simultaneous polarization scrambling measurements discriminated the retinal pigment epithelium from other structures [7,9]. In the anterior eye segment, birefringence of trabecular meshwork and sclera has been used to discriminate individual tissues [10].

Conventional ophthalmic OCT is available from many manufacturers for practical clinical routines. Although PS-OCT is currently not commercially available, a prototype model of PS-OCT has been demonstrated to investigate its *in vivo* clinical applications for the posterior segment of the eye [7,11]. However, a clinical model of PS-OCT for the anterior eye segment has not been demonstrated yet, in spite of its potential clinical applications.

For example, a potential application of PS-OCT for anterior eye segment is the detection of abnormal pterygium fibroblasts that actively grow and synthesize collagen fibrils in tissue. Birefringence of such abnormal fibrous tissue would reveal a region of active growth.

Another potential application is trabeculectomy, which is surgery to reduce intraocular pressure (IOP) with filtering bleb for the treatment of glaucoma. Scarring occurs during wound healing process after the trabeculectomy. Bleb morphology has been investigated to correlate with its functional aspect. Slit-lamp microscope, ultrasound biomicroscope (UBM) and OCT have been used to investigate the structure of blebs [12–16]. However, it has been difficult to diagnose the functioning of the bleb using the conventional imaging methods. PS-OCT may be able to diagnose the scar tissue after the surgery [17].

Since changes in the microscopic organization of fibrous tissues alter the birefringence of tissues, PS-OCT can be used to study microscopic structural changes of the fibrous tissues. The cornea is known to have birefringence [18–25] which results from the highly organized collagen fibrils in the stroma. Abnormalities such as keratoconus which cause the disruption in the organization of collagen fibrils are known to alter the corneal birefringence [25]. Although PS-OCT has been used to investigate the birefringence of keratoconus *ex vivo* [25], *in vivo* measurement of keratoconus has not been demonstrated yet.

In this paper we demonstrate our office-based PS-OCT that has been developed for the clinical applications and discuss its clinical utility based on several cases with various diseases of the cornea and anterior eye segment.

2. Method

2.1. Polarization Sensitive Optical Coherence Tomography System

2.1.1. Hardware Design

The principle of PS-OCT which was employed in the study is similar to a system introduced in our previous paper [26]. Figure 1 shows the schematics (a) and a picture of the PS-OCT (b). This PS-OCT is swept-source OCT based on fiber-based Mach-Zehnder interferometer. The light source was a 30 KHz wavelength sweeping laser (HSL-2000; Santec Corp., Aichi, Japan) which sweeps over 110 nm across a center wavelength of 1.3 μm. These properties of the light source determine the depth resolution of the system, which was measured to be 12.7 μm in air. The polarization state of the light source was continuously modulated by an electro-optic modulator (PC-B3-00-SFAP-SFA-130-UL; EOspace, WA). The modulated light is then split by a fiber coupler (10202A-90-FC; Thorlabs, NJ) into a sample arm and a reference arm with a ratio of 90:10. A mirror is used to reflect the light at the reference arm into a polarization diversity detection arm. At the sample arm, light is split by a pellicle beam splitter (CM1-BP5; Thorlabs) so that 92% of the light is projected on the sample and 8% of the light illuminates a phase reference glass plate. This phase reference glass plate is utilized to stabilize the phase of OCT signal among A-scans. The details have reported elsewhere [26]. The sample arm collects the backscattered light from the sample and the light reflected from the phase reference glass plate. The collected light interferes with the light returning from the reference arm at a non-polarization beam splitter (NPCH-20-13000; Sigma Koki, Tokyo, Japan) in the detection arm. The interference signal is then split by a polarization beam splitter (10FC16PB.7; Newport, CA) into vertically and horizontally polarized components. Two

pairs of orthogonally polarized interference signals are balanced and each detected by one of the two balanced photodetectors (BPD-200; Santec Corp.), respectively.
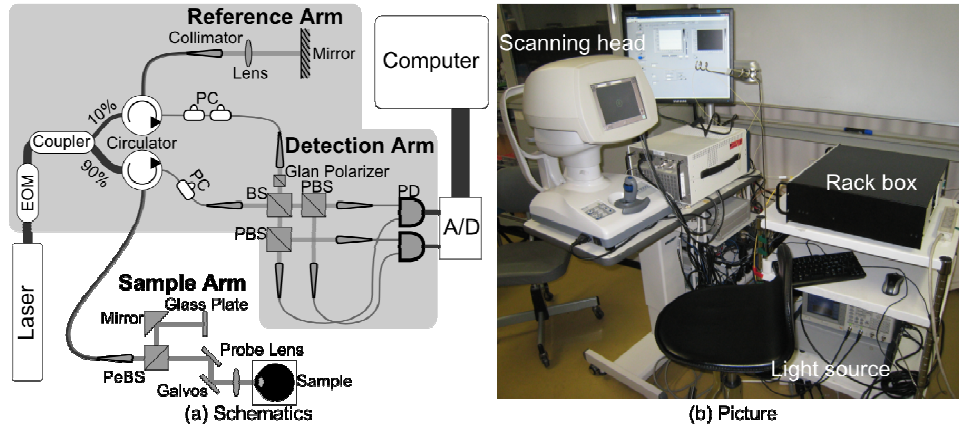

Fig. 1. (a) Schematics and (b) picture of PS-OCT. A/D: Digitizer, BS: Beam splitter, EOM: Electro-optic modulator, PBS: Polarization beam splitter, PC: Polarization Controller, PD: Photodetector, PeBS: Pellicle beam splitter. Components within shaded area were packed in a 402 mm × 452 mm standard rack box. All optical components are connected with single mode fibers, except the free space detection arm.

Since the system was built to use in clinics, the system was designed to be safe, compact and stable. The optical power illuminating the subjects is 3.0 mW, which is below the laser safety limits drawn by American National Standards Institute (ANSI). As shown in Fig. 1(b), all optical components were packed into 3 independent units, namely a light source, a rack box which includes the interferometer, and a custom made motorized scanning head optimized for anterior eye, and these units are connected with optical fibers. The measurement will be stable if the bending of the connection fibers among the 3 units is static, as is true during a single volumetric measurement. The components within the shaded area in Fig. 1(a) were mounted into a 402mm × 452 mm rack box (RBX32/M; Thorlabs) for protection and portability. The probe and the phase reference glass plate of the sample arm are unified and rigidly mounted into the motorized scanning head, which is based on the motorized stage of CASIA anterior OCT (Tomey Corp., Aichi, Japan). By integrating this scanning head, which provides a joystick controlled probe and target monitoring system, positioning of targets becomes more accurate and operation of the system become easier than the 1st generation custom-made probe employed in our previous PS-OCT described in [26].

As described in our previous paper, our PS-OCT operates on condition that the polarization state of the reference arm is linearly polarized at 45 degrees after modulation. To satisfy this condition, a Glan-Laser calcite polarizer (GL5-C26; Thorlabs) was placed in the reference path of the detection arm as shown in Fig. 1(a), whereas it was placed at a reference arm in our previous system.

In the sample arm, a collimated beam with a diameter of 2.9 mm is introduced into an objective lens with a focal length of 61 mm. According to these parameters, the lateral resolution and the depth-of-focus are expected to be 20.5 μm and 5.3 mm, respectively. Note that this depth-of-focus is larger than the system imaging depth of 5.2 mm. The sensitivity of the system was measured to be 98 dB at a depth of 141 μm from the zero-delay, and the sensitivity roll-off was −1.3 dB/mm. This PS-OCT finally provides a Jones matrix tomography in which each pixel represents a Jones matrix of the corresponding point of the sample.

2.1.2. Improvement of Image Quality by Complex Moving Average of Jones Matrices

The image quality of phase retardation is important to visualize clinical data measured by PS-OCT. High signal-to-noise ratio (SNR) is mandatory, especially for accurate phase retardation

imaging [27]. In order to improve the SNR and the image quality of phase retardation images, we employed a custom algorithm of complex moving averaging for Jones matrices. It should be noted that this complex averaging improves the SNR, but with a small penalty of resolution. And hence the kernel size of the averaging should be carefully selected.

Since the Jones matrix at each pixel has different phase offset caused by sub-wavelength randomness of the location of a scatterer, so called global phase [28], it has to be canceled prior to the complex moving averaging. In order to formulate this issue, we define a Jones matrix as

$$\mathbf{J}_n = \begin{pmatrix} a_n & b_n \\ c_n & d_n \end{pmatrix} = \exp(i\beta_n)\begin{pmatrix} a'_n & b'_n \\ c'_n & d'_n \end{pmatrix} \tag{1}$$

where subscript of n indicates *n*-th pixel within a small moving averaging kernel, β_n shows a global phase of the Jones matrix of the *n*-th pixel that depends on the sub-wavelength position of each scatterer. The elements of $\mathbf{J}_n$ are thought to be rotated in respect to those of $\mathbf{J}_1$ in a complex plane as depicted in Fig. 2. This rotation angle is the global phase difference which should be canceled. For the cancelation, we define the rotation angle as

$$\begin{aligned}\beta_n - \beta_1 = \angle \Big\{ &\left(|a_1|^{-1} + |a_n|^{-1}\right)^{-1} \exp\left(i\left(\theta_{an} - \theta_{a1}\right)\right) + \left(|b_1|^{-1} + |b_n|^{-1}\right)^{-1} \exp\left(i\left(\theta_{bn} - \theta_{b1}\right)\right) \\ &+ \left(|c_1|^{-1} + |c_n|^{-1}\right)^{-1} \exp\left(i\left(\theta_{an} - \theta_{a1}\right)\right) + \left(|d_1|^{-1} + |d_n|^{-1}\right)^{-1} \exp\left(i\left(\theta_{bn} - \theta_{b1}\right)\right) \Big\}\end{aligned} \tag{2}$$

Namely, we define the rotation angles relative to $\mathbf{J}_1$ for all pixels in the small region of moving kernel. Since $\mathbf{J}_1$ should have high signal-to-noise ratio (SNR) for reliable calculation, we select a pixel that has the highest combined SNR within the kernel. The combined SNR is defined as

$$SNR_{\mathbf{J}_1} = \left(\tfrac{1}{4}\left(SNR_{a_1}^{-1} + SNR_{b_1}^{-1} + SNR_{c_1}^{-1} + SNR_{d_1}^{-1}\right)\right)^{-1} \tag{3}$$

Each Jones matrix is divided by $\exp\{i(\beta_n - \beta_1)\}$ to compensate the global phase. After this compensation, complex moving averaging is applied.

In this paper, phase retardation images were obtained by moving-averaged Jones matrices, followed by diagonalization of the averaged matrix as described in our previous paper [26].
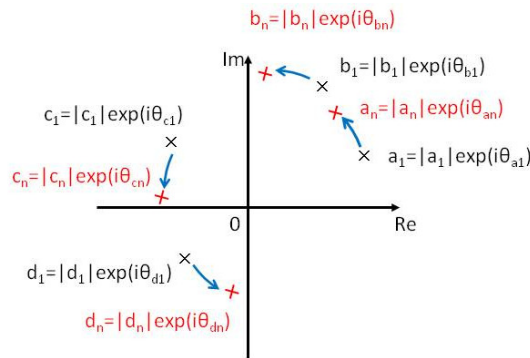

Fig. 2. Rotation of each element of Jones matrix in a complex plane.

2.2. Subjects and Protocols

Five trabeculectomy blebs of 5 glaucoma cases, 1 pterygium eye of a single case, 3 keratoconus eyes of 3 cases and 2 keratoplasty corneas of 2 cases were scanned by PS-OCT.

Four eyes from two rabbits were also used to study birefringence formation in trabeculectomy bleb in detail. Three of the eyes were trabeculectomy models and one was

used as a control. The rabbit eyes were scanned by PS-OCT, and then histological investigation was performed. The 3 rabbit model eyes were measured postoperatively on day 0, 8, and 14. The procedure of trabeculectomy performed on the rabbits is described as follows. The incision of the limbal conjunctiva was made from the 12-o'clock position to the 2-o'clock position, and then a 2×2 mm triangular scleral flap centered at 1-o'clock was created. An area of 0.5×1.5 mm corneal-scleral tissue block was dissected. Finally, the top corner of the triangular scleral flap was sutured.

Keratoconus and keratoplasty eyes were scanned with a horizontal-fast raster pattern on an area of 4×4 mm^2 (512 (horizontal) $\times$ 128 (vertical) A-lines), and 12×12 mm^2 (512 (horizontal) $\times$ 128 (vertical) A-lines), respectively. A control cornea without marked disorder was also scanned by a horizontal raster pattern of 4×4 mm^2 (512 (horizontal) $\times$ 128 (vertical) A-lines). The pterygium was scanned for 10 sequential horizontal B-scans at the same location with the scanning range of 8 mm (1024 A-lines). A vertical-fast raster scan pattern of 12×12 mm^2 (512 (vertical) $\times$ 128 (horizontal) A-lines) 8×8 mm^2 (512 (vertical) $\times$ 128 (horizontal) A-lines) were utilized for the blebs of glaucoma cases and rabbit eyes, respectively.

As mentioned in section 2.1.2, Jones matrices were processed with complex moving averaging with a kernel size of 3×5 pixels before calculating a phase retardation image. For all images, the axial physical size of the kernel was 42 μm. The lateral kernel size depends on scanning density, and was 23, 23, 70, 23, 70, and 47 μm respectively for control cornea, keratoconus, keratoplasty, pterygium, blebs of glaucoma cases and rabbit eyes, respectively.

3. Results

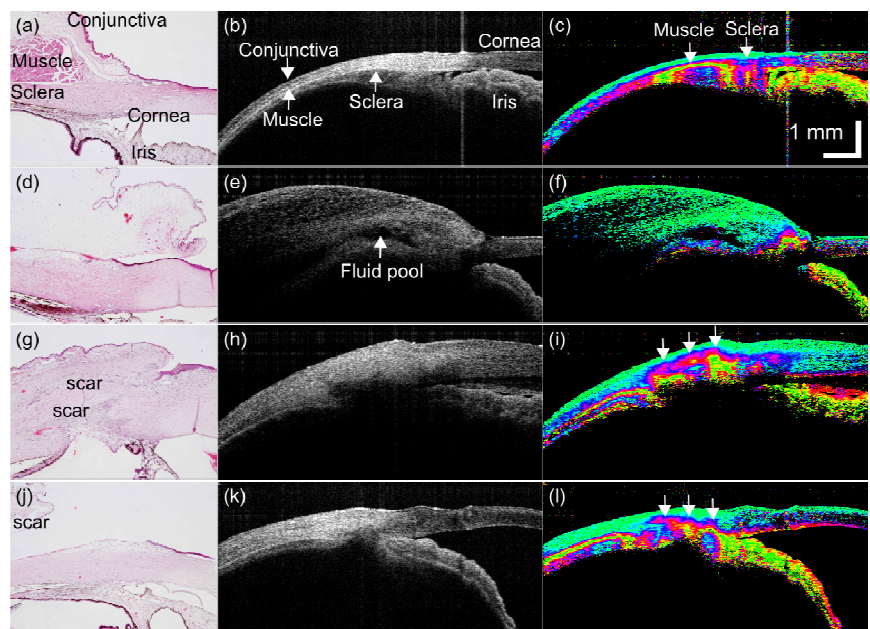### 3.1. Trabeculectomy Model of Rabbits

Fig. 3. (a), (d), (g), (j) Histology images, (b), (e), (h), (k) intensity images, and (c), (f), (i), (l) phase retardation images of rabbit trabeculectomy model. (a)–(c) Control eye. Postoperative day (d)–(f) 0, (g)–(i) 8, and (j)–(l) 14.

Figure 3 shows the PS-OCT images and histological cross-sections of 1 control eye and 3 eyes of rabbit model of trabeculectomy. Figures 3(a), 3(d), 3(g) and 3(j) show histological cross-sections, Figs. 3(b), 3(e), 3(h), and 3(k) show polarization diversity (scattering) OCT, and Figs. 3(c), 3(f), 3(i), and 3(l) show phase retardation images. Note that the scattering OCT and phase retardation images were created from the same spectral data set, and hence perfectly

registered to each other, while the histology was taken from a site in the eye not perfectly registered to but close by the OCT. Figures 3(a)–3(c), 3(d)–3(f), 3(g)–3(i), and 3(j)–3(l) were taken from a control eye, and post-operative eyes on day 0, 8, and 14, respectively.

In the histology image of the control eye (Fig. 3(a)), cornea, conjunctiva, muscle, sclera, and iris were identified as labeled. These tissues were perceived also in the scattering image. In the phase retardation image of Fig. 3(c), strong birefringence was found at the muscle and inhomogeneous birefringence in the sclera. The muscle is appeared as a dark band in the corresponding intensity image (Fig. 3(b)). This dark appearance of ocular muscle is consistent with a previous report [29]

Figures 3(d)–3(f) were taken immediately after the surgery (day 0). A fluid pool of a bleb was found in the scattering OCT (arrow in Fig. 3(e)), consisting of a large cavity with hypo-reflective appearance. No abnormal birefringence was found in the phase retardation image (Fig. 3(f)) and no evident scarring was found in the histology (Fig. 3(d)). Note that the vast green region above the flood pool in the phase retardation image is swelled conjunctiva and nictitating membrane. Since this OCT scan was performed immediately after the surgery, this severe swelling could be reasonable.

In the post-operative eyes of day 8 (Figs. 3(g)–3(i)), and day 14 (Figs. 3(j)–3(l)), collapsed blebs were observed. In the phase retardation images (Figs. 3(i) and 3(l)), abnormal strong birefringence was found at the location of the blebs (arrows). The histological cross-sections indicated that the strong birefringence is the indicator of bleb scarring.

3.2. Human Trabeculectomy

Five blebs of 5 trabeculectomy cases were scanned by PS-OCT. These 5 cases are referred as cases A to E as shown in Fig. 4. The IOPs of the cases A to E were 10, 13, 16, 22, and 32 mmHg, respectively. In this paper, we consider a bleb which has IOP in a range from 10 to 21 mmHg as a functioning bleb. Based on this definition, cases A and B are classified as functioning blebs, and cases C, D, and E are classified as non-functioning blebs.

As shown in Fig. 4(a), multiple microcysts and a large fluid pool were observed in case A. In the phase retardation image (Fig. 4(b)), the sclera showed strong birefringence. However, no abnormal birefringence was found around the fluid pool.

The case B presented a diffusely thickened conjunctiva which appeared as a large moderately hypo-reflective area consisting of several small cavities as shown by scattering OCT (Fig. 4(c)). Also in this case, the birefringence was only found in sclera and no abnormal birefringence was observed (Fig. 4(d)).

In Fig. 4(e) of case C, a large fluid pool surrounded by hyper-reflective tissue was observed. Despite of this hyper scattering appearance, it was not possible to determine the normality of this tissue from this scattering OCT. In contrast, the corresponding phase retardation image (Fig. 4(f)) presented strong birefringence above the fluid pool (arrow). According to the general anatomy of a bleb, the tissue above a normal bleb should be conjunctiva and should not possess birefringence. Hence this appearance in Fig. 4(f) indicates abnormal birefringence.

A fluid pool with a thin wall was observed with case D as indicated by an arrow in Fig. 4(g). In the corresponding phase retardation image (Fig. 4(h)) a vast region with strong birefringence was found. According to the general anatomy of filtering bleb, this birefringence is believed not to be originated from the sclera, hence it is abnormal birefringence.

Case E was a collapsed bleb as shown in Fig. 4(i). In this bleb, a fluid pool is totally corrupted and cannot be observed. The whole region presented irregular and abnormal birefringence as shown by the corresponding phase retardation images (Fig. 4(j)).
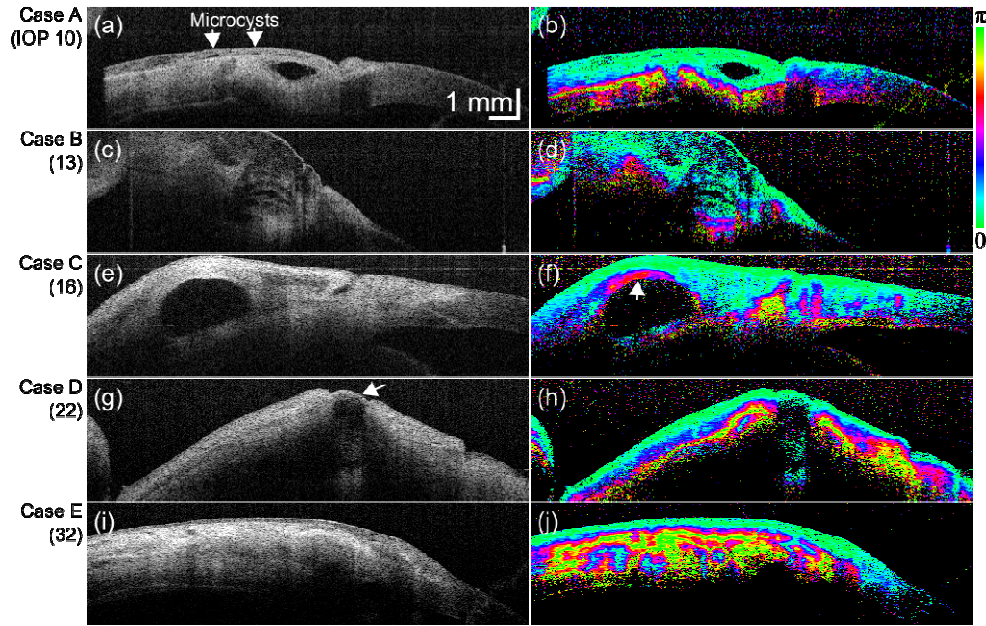
Fig. 4. (left) Scattering OCT and (right) phase retardation images of trabeculectomy cases A–E.

3.3. Pterygium

Figure 5 shows the PS-OCT measurement of a pterygium. Pterygium is abnormal growth of fibroblasts and degenerated collagen beneath the conjunctiva that penetrates to the corneal surface. The border of pterygium and cornea was clearly seen in the scattering OCT (Fig. 5(a)) and indicated by arrows. Although a moderately weak scattering area was seen at the tip of the pterygium, no evident contrast was observed. In contrast, strong birefringence appeared at the tip and in the body of the pterygium in the phase retardation image (Fig. 5(b)) as indicated by * and **. The anatomical structure indicates this strong birefringence is not from sclera, and hence this is likely to be an indicator of active growth of fibroblasts and abnormal collagen.
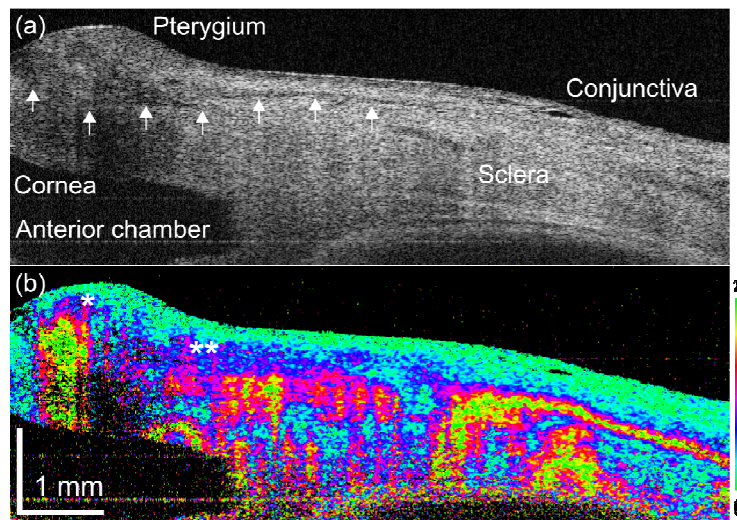

Fig. 5. (a) Scattering OCT and (b) phase retardation images of a pterygium eye.

3.4. Keratoconus

Figure 6 shows 3 cases of keratoconus corneas and 1 case of normal control. Figures 6(a) and 6b) show the control cornea without marked anterior disorder. The scattering OCT does not show evident morphological disorder (Fig. 6(a)). Random phase retardation was observed in the stroma in the phase retardation image (Fig. 6(b)). The mechanism of this random appearance is discussed in section 4.2.

Figures 6(c) and 6(d) are from a case with moderate but noticeable thinning, as indicated by arrows. In the scattering OCT (Fig. 6(c)) the stroma appeared homogenous and the phase retardation shows random appearance (Fig. 6(d)) similar to the control cornea.

Figures 6(e)–6(h) show a case with advanced thinning of the cornea, as indicated by arrows. In the scattering OCT (Fig. 6(e)), the cornea shows corneal opacity which had inhomogeneous hyper-scattering. The corresponding phase retardation image (Fig. 6(f)) shows abnormal and inhomogeneous birefringence as indicated by arrows. The *en face* projection of scattering OCT (Fig. 6(g)) shows a hyper-scattering region at the left-lower part of the cornea, while the *en face* phase retardation map of the posterior surface of the cornea (Fig. 6(h)) shows strong and inhomogeneous birefringence in the corresponding region.

One of the cases was a case with a rupture of Descemet's membrane (Figs. 6(i) and 6(j)). In the scattering OCT (Fig. 6(i)), thickening of the cornea due to the rupture was observed, as indicated by arrows. The tissue beneath the stroma shows hyper-reflectivity. In the phase retardation image (Fig. 6(j)), evident abnormal birefringence was observed in the corresponding region.
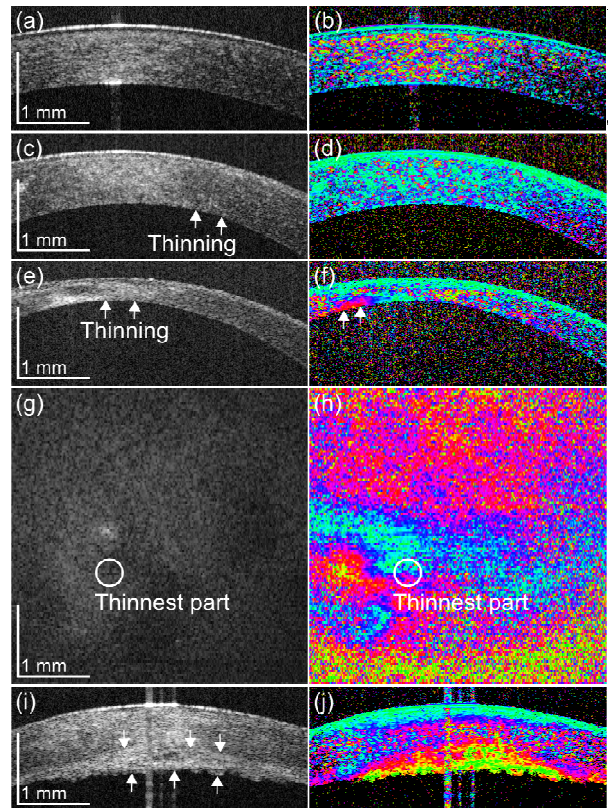

Fig. 6. (left) Intensity images and (right) phase retardation images of (a), (b) a cornea without marked anterior disorder, (c), (d) a cornea with moderate but noticeable thinning keratoconus, (e)–(h) an advanced thinning keratoconus, and (i), (j) a keratoconus with a rupture in the membrane. (g), (h) The posterior surface en face images of the cornea in (e), (f).

3.5. Keratoplasty

Figure 7 represents a case of keratoplasty. In the scattering OCT (Fig. 7(a)), the graft is observed at the center and which is sutured to the host. At the graft-host interface (arrows), moderate thickening and rupturing of the epithelium were observed. Although moderate hyper-scattering was shown, evident alteration of cornea was not clearly observed. In contrast, the phase retardation image (Fig. 7(b)) showed strong birefringence at the graft-host interface. This is an indicator of microstructural alteration of collagen.
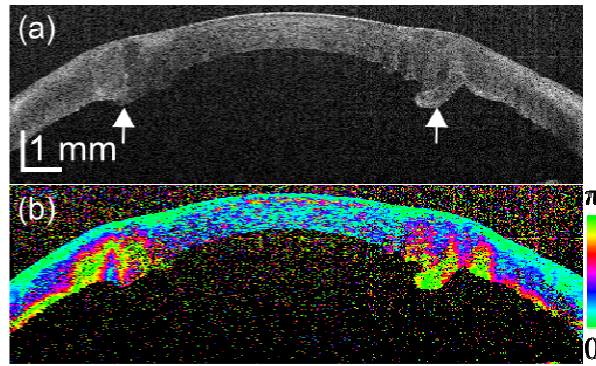

Fig. 7. Intensity images and phase retardation images of keratoplasty patients.

4. Discussion

4.1. Trabeculectomy and Scarring

The OCT measurements of trabeculectomy model in rabbits showed that the blebs with scarring exhibited abnormal birefringence. These results suggest that the appearance of abnormal birefringence can be considered to be an indicator of scarring.

In the measurement of human cases of trabeculectomy, no abnormal birefringence was observed in the functioning blebs, namely cases A, and B, suggesting that no scarring occurred in these blebs. On the other hand, the non-functioning blebs of cases C, D, and E showed abnormal birefringence and the scar spread over a larger area in the blebs D, and E compared to bleb C. This does not contradict the higher IOPs of these cases.

These studies of rabbit model and human cases suggest that PS-OCT is useful to evaluate the function of trabeculectomy bleb, and may be utilized for the planning of secondary surgery.

4.2. Cornea and Cross-Link of Collagen Fibrils

Eyes without marked anterior disorder showed homogeneous random appearance in the phase retardation. This appearance is believed to be caused by low SNR in the stroma. The birefringence measurement method employed in our PS-OCT is sensitive to SNR, and in a low SNR region, such as a normal transparent cornea, the phase retardation appeared random.

Abnormal birefringence was found in the advanced keratoconus cases with evident thinning, and in a case with a rupture of Descemet's membrane. The appearance of abnormal birefringence in these cases was believed to be caused by cross-linking of collagen fibers. Abnormal birefringence was found in a region not at the thinnest part of the cornea and different pattern in the *en face* maps of intensity OCT and phase retardation image suggest that phase retardation image provides additional information about the optical properties in the tissue compared to conventional OCT. This information may be useful to study and diagnose the abnormalities of the cornea.

In the measurement of keratoplasty patients, abnormal birefringence was observed in the cornea around the graft-host interface. The abnormal birefringence was believed to be caused by cross-linking of collagen fibers. This can be utilized as an indicator of this cross-linking in the diagnosis.

5. Conclusion

In conclusion, visualizing the birefringence of tissue by using PS-OCT enabled selective visualization of abnormalities, e.g. scarring and cross-linking of collagen. These findings suggest that PS-OCT is a powerful tool to study and diagnose abnormalities in the cornea and anterior segment.

Acknowledgments